RSC Advances

RSC Advances

www.rsc.org/advances

ROYAL SOCIETY OF CHEMISTRY

www.rsc.org/advances

TOC

Facile and economical synthesis for "Plum Pudding" shaped porous LiFePO$_4$ /carbon composites for lithium ion batteries

Hairong Xue[a], Jianqing Zhao[b], Tao Wang[c], Hu Guo[a], Xiaoli Fan[a], Jianping He[a, *]

[a] College of Material Science and Technology, Nanjing University of Aeronautics and

Astronautics, Yudao Street 29, 210016 Nanjing, PR China.

[b] Louisiana State University, Department of Mechanical and Industrial Engineering, Baton

Rouge, LA 70803, United States.

[c] World Premier International Research Center for Materials Nanoarchitectonics, National

Institute for Materials Science, 1-1 Namiki, Tsukuba, Ibaraki 305-0044, Japan.

*Corresponding author. Tel: +86 25 52112900; Fax: +86 25 52112626.

E-mail address: jianph@nuaa.edu.cn
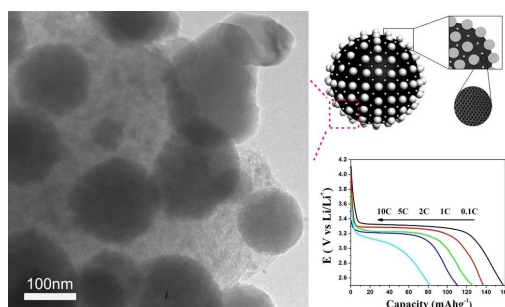
The LiFePO$_4$/C composite shows plentiful LiFePO$_4$ nanospheres uniformly lodged in 3D porous conductive carbon framework and exhibits improved electrochemical performance.

RSC Advances

ARTICLE

Facile and economical synthesis for "Plum Pudding" shaped porous LiFePO4 /carbon composites for lithium ion batteries

Hairong Xue[a], Jianqing Zhao[b], Tao Wang[c], Hu Guo[a], Xiaoli Fan[a], Jianping He[a], *

A facile and economical template-free method has been developed to prepare "Plum Pudding" shaped porous LiFePO4/C electrode materials for lithium ion batteries, which is synthesized by facile and economical one-step dry ball milling with inexpensive Fe^{3+} salt as raw material assisted by carbothermal reduction. Compared with the sample by ball milling with water, dry ball milling is beneficial to homogeneous nucleation of LiFePO4 in drying and subsequent thermal treatment process, so this significant material shows plentiful LiFePO4 nanospheres (~200 nm) uniformly lodged in the 3D porous carbon architectures as an interconnected conductive framework due to the dry ball milling process. For this innovative and available structure, the sample with dry milling possesses nanoscale active electrode materials (an average size distribution of ~200 nm) with increased crystallinity, high surface area (up to 140 m^2 g^{-1}) and enhanced electronic conductivity contribute to improve the rate capability of the battery. The capacity of this "Plum Pudding" shaped porous LiFePO4/C electrode materials achieved 157.4 mAh g^{-1} (92.6% of the theoretical capacity) at the 0.1 C discharge rate and the practical charge capacity has been achieved 154.4 mAh g^{-1} after 100 cycles.

Introduction

The main text of the article should go here with headings as appropriate. LiFePO4 has recently been attracting a great deal of attention as a promising substitute for $LiCoO_2$ due to its potential use.[1-3] As a new cathode material for lithium rechargeable batteries, LiFePO4 has many advantages over conventional cathode materials, such as high competitive theoretical capacity (170 mAh g^{-1}), stable voltage (3.4 V), low cost, environmentally benign, and safety.[4, 5] Therefore it has been used in batteries as electric vehicles (EVs) and hybrid electric vehicles (HEVs).[6-9] However, the low intrinsic electrical conductivity and the sluggish Li^+ diffusion across the LiFePO4/FePO4 interface have limited its application in high power density batteries .The poor high-rate performances of pure LiFePO4 make LiFePO4 cathodes difficult to make full use of them in lithium rechargeable batteries.[10-13] Thus far, many approaches have been adopted to improve the electrical conductivity and Li^+ diffusion capability of LiFePO4 by selective doping supervalent cations in Fe-sites,[6, 10-11] reducing the particle-size to sub-micron and even nano-scale,[12, 14] creating an ion-conducting surface phase (such as $Li_4P_2O_7$),[12] and coating the LiFePO4 particles with electronically

conductive agents such as carbon,[3, 15-20] metals or metal oxides,[21-23] conductive polymer[24] and so on.

The electrochemical performance of electrode materials is closely related to its surface area, particle size and distribution, particulate morphology, carbon content, carbon morphology, phase purity, and so on.[25-27] From the previous publications,[3, 15-20] the 3D architecture has been considered as an alternative optimum structure design of electrode materials. The benefits may be realized for this structure, which improvement sin energy per unit area and high-rate discharge capabilities. Among the different 3D architectures for LiFePO4 cathode materials, the 3D porous carbon framework architectures combining host LiFePO4 particles into one incorporated entity for lithium ion storage can be effective. The use of 3D porous carbon framework has several advantages.[3, 15-20] (i) the growth of LiFePO4 particles can be significantly restricted on the nanoscale so as to shorten the diffusion route of lithium ions by the solid carbon architecture in synthesis and this 3D porous carbon framework also effectively prevent unfavorable aggregations of active material particles; (ii) the strain on or from LiFePO4/FePO4 two-phase transformation also could be released by the rigid carbon skeleton during the lithium ion insertion/extraction; (iii) one more important feature of the

carbon framework is to slow or prevent detrimental corrosion processes in lithium ion batteries; (iv) the excellent inter-particle electronic conductivity and the continuous high surface area porous network allows an efficient transport route for electrolyte through out the electrode and hence may offer high energy and power capacities in lithium ion batteries. Among the various methods used to create this versatile porous carbon framework for lodging $LiFePO_4$ nanoparticles, template approaches have been employed.[16-18, 28-30] Doherty *et al.*[17] reported the preparation of hierarchically porous monolithic $LiFePO_4$/C composite by nanocasting templating technique. This composite monolith electrode attained capacities of 140 mAh g^{-1} at a discharge rate of 0.1 C and 100 mAh g^{-1} at 5 C. However, the preparation of meso/macroporous silica monolith and a chemical etch of the monolith after carbonizing is time consuming. They also used colloidal crystal as a template to produce hierarchically porous $LiFePO_4$.[16] The authors succeeded in preparing electrode materials with the largest pores, around 100 nm in diameter, which showed better discharge capacities for $LiFePO_4$ of 160 mAh g^{-1} at 0.1 C and 115 mAh g^{-1} at a fast discharge rate of 5 C. Nevertheless, this process is very complex, which include the preparation of PMMA colloidal crystal template. So template approaches, using triblock copolymer,[16, 18] citric acid,[28] and other hard or soft templates,[17, 29-30] always are difficult to expand to large-scale commercial applications due to some fatal disadvantages related to high cost and complicated synthetic procedures.[31-32]

Therefore, we develop a one-step template-free methodology for preparing "Plum Pudding" shaped porous $LiFePO_4$/C composites, with $LiFePO_4$ nanospheres within a 3D porous carbon framework. This facile and economical template-free method can allow the mixing of the starting ingredients (inexpensive Fe^{3+} salt) by dry ball milling followed by the carbothermal reduction reaction at 700℃，and glucose was used as the carbon source to produce 3D carbon framework full of macro/mesoporous pores. In order to create this versatile carbon framework, sort of high carbon content is unavoidable, more efforts are being taken to solve this dilemma.[17, 18] The "Plum Pudding" shaped porous $LiFePO_4$/C composites reveal the considerably enhanced electronic conductivity and remarkable high surface area, which may provide materials with interesting properties for applications in lithium ion batteries.

Experimental

Material preparation

 "Plum Pudding" Shaped porous $LiFePO_4$/C composite was prepared via ball milling. The starting materials, $LiAC·2H_2O$, $Fe(NO_3)_3·9H_2O$, $NH_4H_2PO_4$ and glucose, were put into a stainless steel cylindrical container with stainless steel balls. The precursors were mixed by ball-milling at 400 rpm for 4 hours and subsequently aged for 12 hours in tanks after operations. The mixture was initially dried in a vacuum oven at 80 ℃, hand grinded with an agate pestle and mortar and then heated in a nitrogen atmosphere at 700 ℃ for 10 hours. All

heating rates were 5 ℃ min^{-1}. The products were obtained after cooling at room temperature .The molar ratio of Li: Fe: P: C in the precursor was 1:1:1:2. Carbon converted from glucose acted as reducing agent in the synthesis process and conducting agent in the resulting sample, and the carbon content in the LFP-A is 31.2 % (Fig. S1 of Supporting Information). The samples were tried two ways of ball milling, including dry ball milling and ball milling with water, which were labeled as LFP-A and LFP-B, respectively.

Structural and morphological characterization

The crystalline phases of $LiFePO_4$/C samples were identified through X-ray diffraction (XRD) under a Bruker D8 X-ray diffraction meter with monochromatic Cu K radiation (λ = 0.154056 nm). The size and surface morphology of the samples were observed by using a Hitachi S-4800 field emission scanning electron microscopy (FESEM). Transmission electron microscopy (TEM) images were captured on the JEM-2100 instrument microscopy at an acceleration voltage of 200 kV to investigate the diameter and distribution of $LiFePO_4$ particles within the carbon framework as well as the characteristics of the carbon coating layer. Thermogravimetric (TG) measurements of the products were monitored using a NETZSCH STA 409 PC from 30 to 900 °C under oxygen with a heating rate of 10 °C min^{-1}.The porous structures of the samples were measured by an N_2 adsorption isotherm using a Micromeritics ASAP 2010 at 77 K. The specific surface areas were calculated using the Brunauer-Emmet-Teller (BET) method. The Brunauer-Emmett-Teller (BET) method was utilized to calculate   the specific surface areas based on adsorption data in the partial pressure (P/P_0) range 0.05-0.2. The pore volumes and pore size distributions derived from the desorption branches of isotherms were estimated based on Barett-Joyner-Halenda (BJH) model, the total pore volumes (V_{pore}) were computed from the adsorbed amount at a relative pressure (P/P_0) of 0.992.

Electrochemical tests

Test cathodes were prepared by mixing with acetylene black and polyvinylidene fluoride (PVDF) with a weight ratio of 75:15:10 in N-methyl-2-pyrrolidone (NMP) solvent to produce the slurry. After mixing for 24 hours, the resultant viscous slurry was spread into the aluminum current collector and dried at 120 ℃ overnight under vacuum. After rolling, the obtained sheets were cut into circular strips of 16 mm in diameter, and about 3.0 ± 0.1 mg cm^{-2} active materials were loaded on an Al foil. The strips were dried at 80 ℃ for 24 hours. Electrochemical measurements were conducted in Li test cells with lithium foil as counter and reference electrodes. All test cells contained 1.0 mol L^{-1} $LiPF_6$/EC-DEC (1:1 Vol%) as an electrolyte and were assembled in an argon-filled glove box. Galvanostatic charge/discharge reactions were performed in the voltage range of 2.5 ~ 4.2 V on the CT2001A LAND Battery Tester. The electrochemical storage capacities of samples were calculated from the mass of $LiFePO_4$ with the amount of carbon being subtracted. The cyclic voltammetry (CV) of samples

were performed with the scanning rate at 1 mV s^{-1} respectively on the electrochemical workstation (CHI660C). Electrochemical impedance spectroscopy (EIS) measurements using a Solartron 1260 frequency response analyser coupled to a Solartron 1287 potentiostat were obtained at frequencies between 100 kHz and 0.01 Hz. The amplitude of the sinusoidal potential signal was 10 mV.

Results and discussion

Crystalline structure analysis
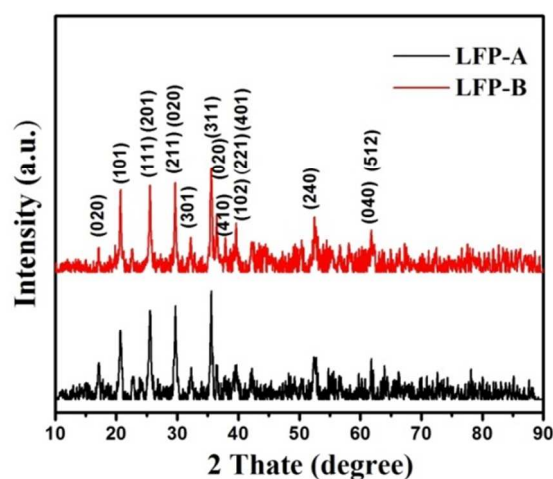
Fig. 1. XRD-patterns of LiFePO4/C composites.

Fig. 1 shows the XRD patterns of LiFePO$_4$/C composites with water or without mediums during ball milling followed by the carbothermal reduction reaction at 700 ℃ . The sharp diffraction peaks of the samples without any obvious impurity phase indicate well-crystallized LiFePO$_4$/C with an olivine type structure is successfully synthesized .All the diffraction peaks can be indexed on the basis of the orthorhombic olivine-type structure (JCPDS No.83-2092) with the Pnma space group. Moreover, widening of the peaks occurs as dry milling was increased, suggesting the decrease in LiFePO$_4$ crystallite diameter, which is in agreement with the result of FE-SEM and TEM images shown in Fig. 2. The lattice constants of the as-synthesized samples are listed in Table 1, similar to the previous report.[1] In addition, the reduced lattice constants indicate that the crystalline growth of LiFePO$_4$ crystals may be restricted due to the hard carbon framework.[20]

Table 1. Structural lattice parameters and cell volumes of LiFePO$_4$/C composites.

Sample	a(Å)	b(Å)	c(Å)	V(Å^3)
Standard pattern	10.347	6.019	4.704	292.9
LFP-A	10.318	6.022	4.699	292.0
LFP-B	10.367	6.020	4.690	292.7

Morphological analysis
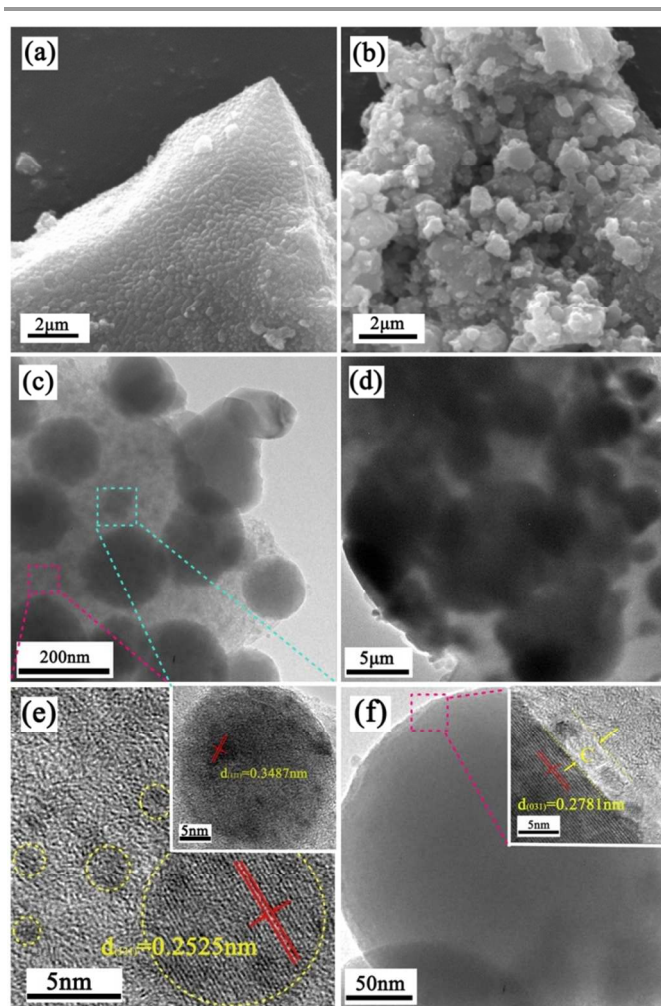
Fig.2. FE-SEM and TEM images of LiFePO$_4$/C composites: (a) (c) LFP-A; (b)(d) LFP-B; (e) (f) TEM and HR-TEM images of LFP-A.

Fig. 2(a) displays an FE-SEM image of the LiFePO$_4$/C composites heat-treated at 700 °C for 10 hours after dry milling. As illustrated in Fig. 2(a), These LFP-A particles can be clearly observed that many densely aggregated LiFePO$_4$ nanospheres cover the surface of the particles. These LiFePO$_4$ nanospheres show a uniform distribution of particle size with an average diameter of ~150 nm. The elemental mappings of C, Fe, P, and O for LFP-A are shown in Fig. S2 (in Supporting Information), indicating a homogeneous distribution of the continuous guest carbon framework and host LiFePO$_4$ lodgers. In contrast, as shown in SEM images in Fig. 2(b), the LFP-B consisted of LiFePO$_4$ nanospheres of about 100-500 nm in diameter, with a larger particle size distribution and a serious agglomeration of LiFePO$_4$ particles, which is consistent with its TEM image (Fig. 2(d)). Furthermore, as disclosed in the TEM image shown in Fig. 2(c), the LFP-A shows significant "Plum Pudding" shape consisting of numerous LiFePO$_4$ nanospheres of about 100-150 nm in diameter uniformly embedded in a carbon matrix. The smaller LiFePO$_4$ nanospheres inside of the samples, especially for LFP-A, indicating that this carbon matrix has a significant effect on the crystal size of LiFePO$_4$

due to its additional role as a barrier layer to restrict $LiFePO_4$ crystal growth during thermal treatment. Besides, the region marked with amaranth and blue rectangle in Fig. 2(c) analyzed by HRTEM is shown in Fig. 2(e), the interspaces of the larger $LiFePO_4$ nanospheres were filled with abundant smaller spheres in the continuous carbon matrix, which contributed to obtain higher tap density of this cathode material to guarantee the high energy density in working electrodes.[20] From the deep observation marked with amaranth rectangle in HRTEM image of Fig. 2(f), it can be seen that the carbon layer closely coated on the surface of $LiFePO_4$ nanosphere of the LFP-A is about 4 nm thick. Meanwhile, a regular fingerprint is shown in the core of the particle, indicating the $LiFePO_4$ particles with a high degree of crystallization. This carbon structure in combination with the perfect carbon coating layer enhances greatly the electronic conductivity of $LiFePO_4$. It is believed that the small particle size of $LiFePO_4$ is useful for the intercalation/de-intercalation process of lithium ions, as the aforementioned $LiFePO_4$ nanospheres. In addition, a large number of studies have shown that lithium ion diffusion kinetics is related to superior high-power electrochemical performance and properties. The ability of lithium ions to travel across the interface between $LiFePO_4$ and electrolyte phases is crucial for ultrafast diffusion, so this perfect carbon coating layer could accelerate the mobility of lithium ions. Therefore, this "Plum Pudding" shaped porous $LiFePO_4$/C composite is very suitable as an electrode material to improve the electrochemical properties of lithium-ion batteries.

Further details regarding porosities of this intriguing $LiFePO_4$/C composite material were obtained through nitrogen adsorption measurements. The nitrogen adsorption/desorption isotherms of both LFP-A and LFP-B composite material exhibited typical IV shapes with H3-type hysteresis loops in Fig. 3(a),[33] revealing the porous characteristic of them all with abundant macro/mesopores. In addition, the adsorption/desorption curves do not level off at relative pressures close to the saturation vapor pressure, suggesting the presence of slit-like pores that might be caused by $LiFePO_4$ nanoparticles. The Barrett-Joyner-Halenda (BJH) desorption pore-size distribution curves of the composite material calculated from the desorption branch were shown in Fig. 3(b), based on the Kelvin equation and corrected for multilayer adsorption. The pore sizes, BET surface areas and pore volumes of materials calculated from the N_2 adsorption-desorption data are summarized in Table 2. In contrast to previous $LiFePO_4$/C products, the BET surface area of these samples is obviously higher, which arrived at over 100 m^2 g^{-1}. This appreciable high BET surface area probably results from the porous carbon framework formed from the vigorous gas evolution produced from decompositions of the precursor (mainly nitrate, ammonium dihydrogen phosphate and organic compounds) during thermal treatment.[20, 32, 34-35] The fact that LFP-A with the higher BET surface area maybe benefit from a relatively regular spherical type with uniform scale of $LiFePO_4$ nanospheres. In addition, nanoscale size of the high dispersed $LiFePO_4$ also benefits the increase of surface area. Overall, the significant porosity in cathode materials can facilitate the access and accommodation of electrolyte and shorten the diffusion length of lithium ions to achieve high power density in electrode materials.
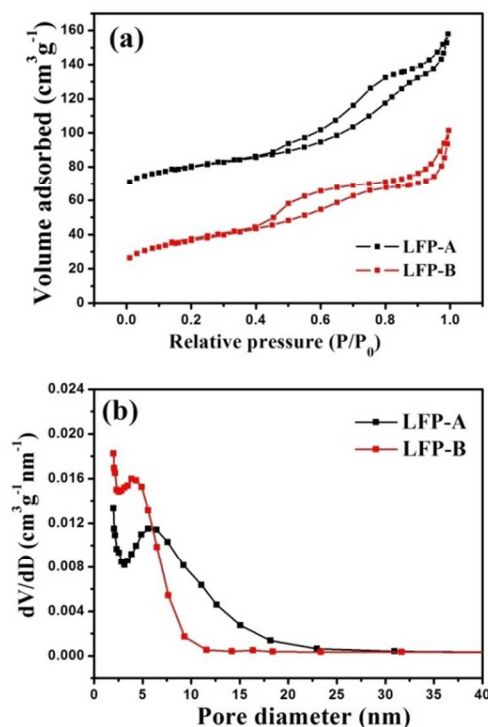
Fig. 3. Nitrogen adsorption/desorption isotherms (a) and pore size distribution curves (b) of $LiFePO_4$/C composites.

Table 2. Pore structure parameters of $LiFePO_4$/C composites.

sample	Specific surface area (m^2 g^{-1})	Pore volume (cm^3 g^{-1})	Aperture(nm)
LFP-A	140.6	0.165	6.5
LFP-B	102.3	0.167	4.7
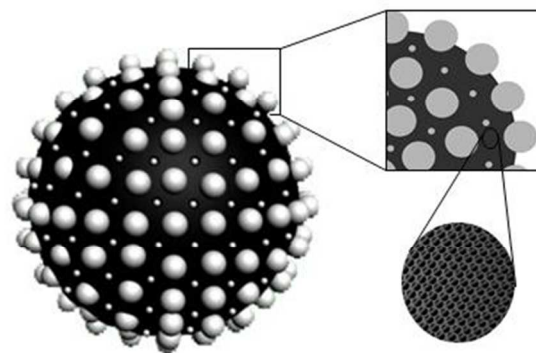
Fig. 4. Schematic diagram of the "Plum Pudding" shaped porous $LiFePO_4$/C composite in the 3D structure.

As discussed above, the LiFePO$_4$/C composite shows that LiFePO$_4$ nanospheres are tightly lodged in the 3D porous carbon framework, it is visible in the schematic diagram in Fig. 4. The formation process of the "Plum Pudding" shaped porous LiFePO$_4$/C composite (LFP-A) can be visualized from following description. The starting materials can be homogeneously mixed by ball-milling, and the sealed stainless steel tanks provide the relatively high temperature and pressure environment after ball-milling, which is beneficial to the initial nucleation of spherical LiFePO$_4$ nanoparticles and formation of the carbon framework.[20,26] In addition, dispersion medium in the ball milling process has an effect on the dispersion of granule and the state of aggregation of the raw material, it leads to a mixture particle reunion state of the pulp after drying, finally influence on the mass transfer process of reactants in the sintering process. As we all know, water is a common polar solvent and possesses high boiling point. So, the higher boiling point is, the slower drying rate is. In the drying process after ball-milling, the augmented and formed speed of particles will be slow, and the componental segregation degree will increase. Therefore, the reunion of particles and segregation degree of compositions are more serious due to the slow drying rate of large amounts of water, thus leading to worse particle distribution. In addition, the sealed stainless steel tanks will provide the relatively high temperature environment in the ball-milling. And ferric nitrate is a special iron source, it has a lot of crystal water and shows low melting point (47.2℃), so it will be melting in the process of ball milling. The molten ferric nitrate and some water derived from crystal water could be as dispersant, which will be beneficial to improve the effect of dry ball-milling. Moreover, because of proportionally less water, drying rate is fast, thus leading to better particle size distribution and more uniform structure by dry ball-milling.

Electrochemical performance
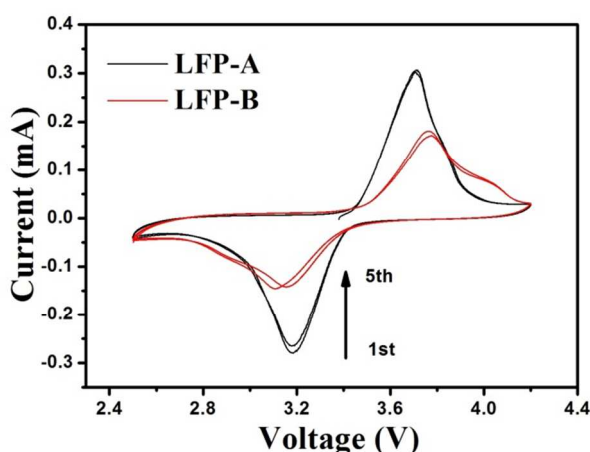
Fig. 5. First and fifth cycles in cyclic voltammograms (CV) determination of LFP-A and LFP-B at a scan rate of 0.1 mV s^{-1}.

The first and fifth cycles in cyclic voltammograms (CV) determination of the as-obtained LiFePO$_4$/C cell tested between 2.5 V and 4.2 V at a scanning rate of 0.1 mV s^{-1} was shown in

Fig. 5. All the samples shown very high peak symmetry, this indicates they all have a good cycle reversibility benefiting from the established 3D porous carbon fabric as a conductive network for ultrafast electron transfer and a capacious container for sufficient electrolyte penetration. The reduction and oxidation peaks in the first cycle of the LFP-A appear at 3.19 V and 3.68 V, this indicates that Fe^{2+}/Fe^{3+} redox pairs contribute to the gain and loss of electrons in the LiFePO$_4$ crystal structures of the sample during the lithium insertion and extraction process .The voltage difference between the oxidation and reduction peaks is 0.48 V. However, in the first cycle CV curve of the LFP-B, the reduction peak is observed at a potential of 3.15 V and the corresponding oxidation peak is observed at 3.77 V, the voltage difference is 0.62 V. It can be found that the CV curve of the LFP-A with dry milling showed the better peak symmetry, the narrower voltage separation. In addition, the reproducibility in CV measurements of the samples was shown in Fig. 5. After four cycles, LFP-A shows much better reproducibility than LFP-B, proving the outstanding reversibility of LFP-A as cathode material. As discussed above, the LFP-A prepared by dry milling exhibited more feebleness polarization, further more lithium ions and electrons are participating actively in redox reactions, allowing reversible electrochemical reactions during extraction and insertion of lithium ions. Moreover, the LFP-A showed the higher peak current density, it is visible in SEM and TEM of LFP-A (Fig. 2), those nanoscale LiFePO$_4$ spheres can provide various advantages in terms of reducing diffusion path of lithium ions and offering more active sites for electrochemical reactions.
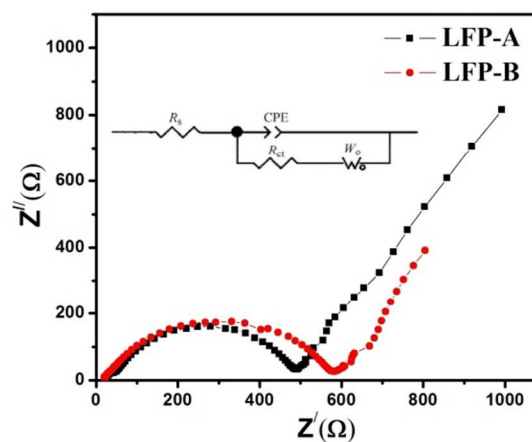
Fig. 6. Electrochemical impedance spectra measurements (EIS) of LFP-A and LFP-B, inset is the equivalent circuit

To further demonstrate the effect of ball milling way in the kinetic process of the electrode materials, electrochemical impedance spectra measurements (EIS) were carried out in three two-electrode coin cells under discharging platform condition. Fig. 6 shows the EIS data of the samples of LiFePO$_4$/C with and without solvent. The corresponding equivalent circuit is proposed to fit the impedance plots as seen in the inset image of Fig. 6. R_s is caused by the liquid phase

ohmic resistance when charges transfer from the counter electrodes to the electrolyte, the constant phase element (*CPE*) represents the charge-transfer process at the electrolyte/electrode interface, R_{ct} is due to charge-transfer resistance, W_o is caused by the inhomogeneous diffusion impedance, and W_0-T is the Warburg coefficient. The fitting parameters using Zview impedance analysis software 2.80 are shown in Table 3.

Table 3. Fitted results of electrochemical impedance spectra of LiFePO₄/C composites.

Sample	$R_s(\Omega)$	$CPE(\mu F)$	$R_{ct}(\Omega)$	W_o-T
LFP-A	25.8	24.0	483	0.35
LFP-B	19.7	10.5	550	0.32

All the EISs are comprised of an intercept at high frequency followed a depressed semicircle in the middle-high frequency region and a sloping line in the low frequency. The high frequency intercept represents the ohmic resistance (*Rs*) at the real axis, while the semicircle middle-high frequency region basically deals with the complicated reactions occurring at the

interface of electrolyte-electrode, which mainly includes the charge-transfer resistance of electron and lithium-ion (*Rct*) and corresponding capacities (*CPE*). The sloping line ascribes the Warburg impedance (W_0), associated with lithium-ion diffusion through the LiFePO₄ electrode, as indicated in the inset image of Fig. 6. In the middle-high frequency region, the LFP-A exhibited a smaller charge-transfer resistance while LiFePO₄/C composite prepared from ball milling with water solvent had the largest value. The lower *Rct* value of the LFP-A indicates a lower electrochemical polarization and the charge transfer resistance may be the limiting factor for the electrochemistry results, which can be attributed to the smaller particles. The smaller particle size is associated with the lower electronic and/or ionic resistance at the boundary of the crystallites within each polycrystalline particle of the active material, thus improving the reversible capacity of LiFePO₄/C material. Furthermore, narrower particle size distribution and uniform dispersion of the LiFePO₄ nanospheres help to form interconnected carbon framework, which significantly improve the conductivity of the LiFePO₄/C composite.
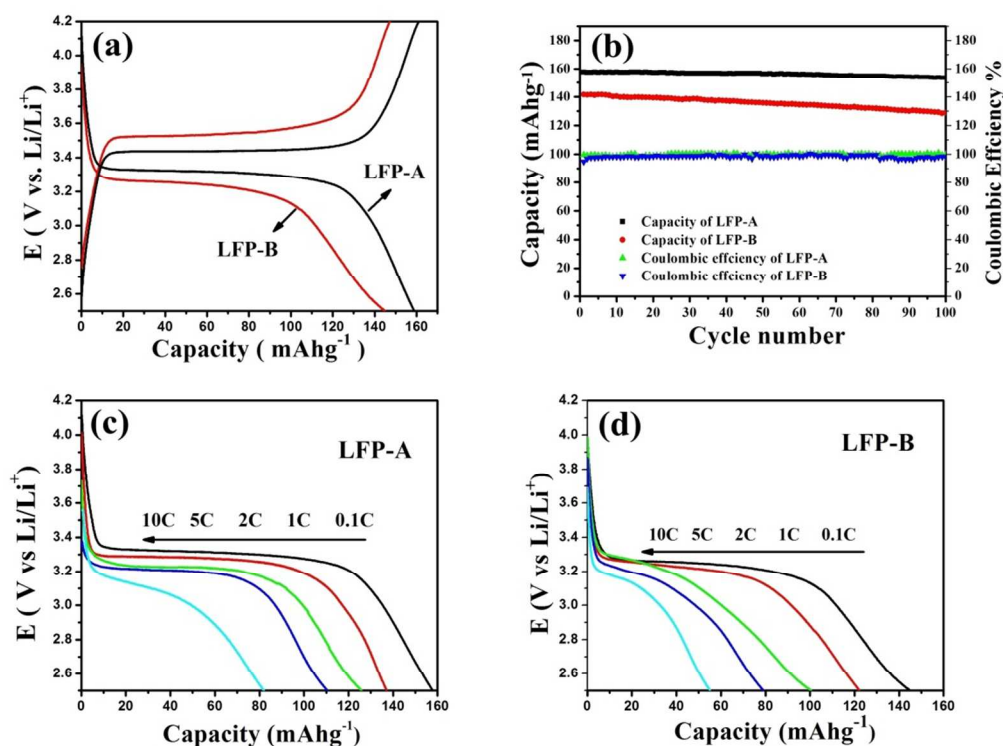
Fig. 7. Electrochemical performance of LiFePO₄/C composites: (a) first charge/discharge curves and (b) cycle performance and Coulombic efficiency curves of LFP-A and LFP-B at 0.1 C; rate capabilities of LEP-A (c)and LFP-B (d), the cells were charged to 4.2 V at 0.1 C and then discharged at various rates.

The first charge-discharge profiles of the LiFePO₄/C samples at 0.1 C rate are shown in Fig. 7(a). For comparison, those of LiFePO₄/C produced by ball milling with water solvent or solvent-free are also shown by dotted lines in the figure. All the samples possess a flat plateau around 3.4 V, corresponding to the two-phase (LiFePO₄↔FePO₄) transformation model. Near the starting and ending discharge, two slopes could be

discovered, attributing to the existence of small single-phase domain as reported by Yamada and co-workers. The LFP-A has a discharge capacity of 157mAh g⁻¹, which corresponds to 92% of the theoretical capacity of LiFePO₄ (170mAh g⁻¹), whereas sample LFP-B shows reduced capacities, 140mAh g⁻¹ for water solvent. Furthermore, the LiFePO₄/C with solvent-free has a much smaller polarization loss and irreversible capacity. Taking

into account the cyclability of the samples, Fig. 7(b) shows remarkable electrochemical cycling stability of LFP-A with less than 6% decay in discharge capacity (better than 94% retention) up to 100 cycles. The LFP-B electrode material had only 89.6% capacitance retention after 100 cycles. Besides, the Coulombic efficiency of the LFP-A is higher than LFP-A, which maintained above 99% for all the charge and discharge processes, confirming the excellent reversibility. Furthermore, the discharge capacities of the $LiFePO_4/C$ composites prepared into electrodes are presented in Fig. 7(c, d), all the samples are cycled five times at various discharge current rates of 0.1 C, 1 C, 2 C, 5 C, and 10 C. The capacity of $LiFePO_4/C$ composite prepared with water solvent decreased quickly with the increase of discharge rate, it is 144, 121, 100, 79 and 56 mAh g^{-1} at the discharge current rate from low to high, respectively. The "Plum Pudding" shaped porous $LiFePO_4/C$ composite (LFP-A) by ball milling for 4 hours with solvent-free in the higher capacities at all investigated discharge rates. It reached 157, 138, 122, 110 and 82 mAh g^{-1} at 0.1, 1, 2, 5 and 10 C discharge rates, respectively. This excellent electrochemical performance is likely due to the structural features of the composite material, with plentiful $LiFePO_4$ nanospheres uniformly lodged in the 3D porous carbon architectures. The fast transport of electron and lithium ion between $LiFePO_4$ nanospheres and electrolyte enhances lithium ion diffusion in $LiFePO_4/C$ composite, which can be ascribed to the 3D porous and equally distributed nanoscale $LiFePO_4$. Moreover, the thin carbon layer coating and the interconnected conductive carbon framework are beneficial to improve the diffusion of electron. Therefore, this "Plum Pudding" shaped porous $LiFePO_4/C$ composite (LFP-A) as cathode material can afford high energy and power densities in lithium ion batteries.

Conclusion

A facile and economical one-step method based on ball milling approach has been established for the synthesis of a composite of the "Plum Pudding" shaped porous $LiFePO_4/C$ composite. The presence of porosity carbon framework architecture for lodging $LiFePO_4$ nanospheres is an effective approach to improve performance of the "Plum Pudding" shaped porous $LiFePO_4/C$ electrode. This unique carbon structure could enhance electrical conductivity by increasing electron transport between $LiFePO_4$ nanospheres and provide abundant porosities allowing the electrolyte to penetrate deep into the electrode material. SEM and TEM observations reveal that the $LiFePO_4$ nanospheres mediated by dry ball milling consist of nearly homogenous nanocrystals with a size of 150~200 nm, while the $LiFePO_4$ nanospheres by ball milling with water comprises some large agglomerates. Galvanostatic test shows that the "Plum Pudding" shaped porous $LiFePO_4/C$ composite exhibits a high electrochemical activity in terms of discharge capacity, cyclability, and rate capability, such as largest reversible capacity of 157.8 mAh g^{-1} at 0.1 C, best rate capability of 84.7 mAh g^{-1} at 10 C, and excellent cyclic stability which retrieves nearly 98.1% of the starting capability in 100th

cycles after discharging at 0.1 C. As such, cathodes fabricated from this composite are promising for high power electrical energy-storage applications such as electric vehicles and power tools.

Conclusions

The conclusions section should come at the end of article, before the acknowledgements.

Acknowledgements

Notes and references

a College of Materials Science and Technology, Nanjing University of Aeronautics and Astronautics, 210016 Nanjing, PR China.
b Department of Mechanical and Industrial Engineering, Louisiana State University, Baton Rouge, LA 70803, United States.
c World Premier International Research Center for Materials Nanoarchitectonics, National Institute for Materials Science, 1-1 Namiki, Tsukuba, Ibaraki 305-0044, Japan.
Tel: +86 25 52112900; Fax: +86 25 52112626.
E-mail address: jianph@nuaa.edu.cn

1   A. K. Padhi, K. S. Nanjundaswamy, J. B. Goodenough, *J. Electrochem. Soc.*, 1997, **144**, 1188-1194.
2   J. M. Tarascon, M. Armand, *Nature*, 2001,**414**, 359-367.
3   Y. T. Xing, Y. B. He, B. H. Li, X. D. Chu, H. Z. Chen, J. Ma, H. D. Du, F. Y. Kang, *Electrochim. Acta*, 2013, **109**, 512-518.
4   Z. Y. Bi, X. D. Zhang, W. He, D. D. Min, W. S. Zhang, *RSC Adv.*, 2013, **3**, 19744-19751.
5   M. Xie, X. X. Zhang, S. X. Deng, Y. Z. Wang, H. Wang, J. B. Liu, H. Yan, J. Laakso, E. Levänen, *RSC Adv.*, 2013, **3**, 12786-12793
6   Y. G. Huang, Y. L. Xu, X. Yang, *Electrochim. Acta*, 2013, **113**, 156-163.
7   R. G. Mei, X. R. Song, Y. F. Yang, Z. G. An, J. J. Zhang, *RSC Adv.*, 2014, **4**, 5746-5752.
8   M. Y. Cho, K. B. Kim, J. W. Lee, H. Kim, H. Kim, K. Kang, K. C. Roh, *RSC Adv.*, 2013, **3**, 3421-3427.
9   T. F. Liu, Li. Zhao, D. L. Wang, J.S. Zhu, B. Wang, C. F. Guo, *RSC Adv.*, 2014,**4**, 10067-10075.
10 S. Y. Chung, J. T. Bloking, Y. M. Chiang, *Nat. Mater.*, 2002, **1**, 123-128.
11 M. Thackeray, *Nat. Mater.*, 2002, **1**, 81-82.
12 B. Kang, G. Ceder, *Nature*, 2009, **458**, 190-193.
13 M. Wagemaker, B. L. Ellis, D. Lützenkirchen-Hecht, F. M. Mulder, L. F. Nazar, *Chem. Mater.*, 2008, **20**, 6313-6315.
14 R. Malik, D. Burch, M. Bazant, G. Ceder, *Nano Lett.* 2010, **10**, 4123-4127.
15 D. Zhao, Y. L. Feng, Y. G. Wang, Y. Y. Xia, *Electrochim. Acta*, 2013, **88**, 632-638.
16 C. M. Doherty, R. A. Caruso, B. M. Smarsly, C. J. Drummond, *Chem. Mater.*, 2009, **21**, 2895-2903.
17 C. M. Doherty, R. A. Caruso, B. M. Smarsly, P. Adelhelm, C. J. Drummond, *Chem. Mater.* 2009, **21**, 5300-5306.

18 X. L. Wu, L. Y. Jiang, F. F. Cao, Y. G. Guo, L. J. Wan, *Adv. Mater.* 2009, **21**, 1-4.

19 F. Y. Cheng, Z. L. Tao, J. Liang, *J. Chen, Chem. Mater.* 2008, **20**, 667-681.

20 J. Q. Zhao, J. P. He, J. H. Zhou, Y. X. Guo, T. Wang. S. C. Wu, X. C. Ding, R. M. Huang, H.R. Xue, *J. Phys. Chem. C*, 2011, **115**, 2888-2894.

21 F. Croce, A. D'Epifanio, J. Hassoun, A. Deptula, T. Olczac, B. Scrosati, Electrochem. *Solid-State Lett.*, 2002, **5**, A47-A50.

22 S. Franger, F. L. Cras, C. Bourbon, H. Rouault, Electrochem. *Solid-State lett.*, 2002, **5**, A231-A233.

23 Y. G. Wang, Y. R. Wang, E. Hosono, K. X. Wang, H. S. Zhou, *Angew. Chem. Int. Ed.*, 2008, **47**, 7461-7465.

24 Y. H. Huang, J. B. Goodenough, *Chem. Mater.* 2008, 20, 7237-7241.

25 S. Ferrari, R. L. Lavall, D. Capsoni, E. Quartarone, A. Magistris, P. Mustarelli, P. Canton, *J. Phys. Chem. C*, 2010, **114**, 12598-12603.

26 X. Qin, X. H. Wang, H. M. Xiang, J. Xie, J. J. Li, Y. C. Zhou, *J. Phys. Chem. C* 2010, **114**, 16806-16812.

27 A. V. Murugan, T. Muraliganth, A. Manthiram, *J. Phys. Chem. C*, 2008, **112**, 14665-14671.

28 F. Yu, J. J. Zhang, Y. F. Yang, G. Z. Song, *J. Power Sources*, 2009, **189**, 794-797.

29 S. Lim, C. S. Yoon, J. Cho. *Chem. Mater.*, 2008, 20, 4560-4564.

30 G. X. Wang, H. Liu, J. Liu, S. Z. Qiao, G. Q. M. Lu, P. Munroe, H. J. Ahn. *Adv. Mater.*, 2010, **22**, 4944-4948.

31 J. F. Qian, M. Zhou, Y. L. Cao, X. P. Ai. H. X. Yang, J. *Phys. Chem. C*, 2010, **114**, 3477-3482.

32 B. J. Hwang, K. F. Hsu, S. K. Hu, M. Y. Cheng, T. C. Chou, S. Y. Tsay, R. Santhanam. *J. Power Sources*, 2009, **194**, 515-519.

33 S. J. Gregg, K. S. W. Sing, Adsorption, Surface area, and Porosity. Academic Press: London, 1976.

34 R. Dominko, M. Bele, J. M. Goupil, M. Gaberscek, D. Hanzel, I. Arcon, Jamnik, J. *Chem. Mater.*, 2007, **19**, 2960-2969.

35 J. K. Kim, J. W. Choi, G. S. Chauhan, J. H. Ahn, G. C. Hwang, J. B. Choi, H. J. Ahn, *Electrochim. Acta*, 2008, **53**, 8258-8264.